Design of binderless grinding wheel with positive rake angle and fabrication used femtosecond laser ablation for grinding soft and brittle crystals

Qu, M., Jin, T., Xie, G., Cai, R. & Lu, A.

DOI 10.1016/j.optlaseng.2019.105803
ISSN 0143-8166

Publisher: Elsevier

Design of binderless grinding wheel with positive rake angle and fabrication used femtosecond laser ablation for grinding soft and brittle crystals

Meina Qu[a, b], Tan Jin[a, b], Guizhi Xie[a,b,*], Rui Cai[c], Ange Lu[a, b]

[a] National Engineering Research Centre for High Efficiency Grinding, Hunan University, Changsha, Hunan 410082, China

[b] College of Mechanical and Vehicle Engineering, Hunan University, Changsha, Hunan 410082, China

[c] School of Mechanical, Aerospace and Automotive Engineering Faculty of Engineering Environment and Computing, Coventry University, 3 Gulson Road, Coventry, CV1 2JH, UK

* Corresponding author. Tel.: +86 731 88821833; fax: +86 731 88823921. E–mail address: guizhixie@hnu.edu.cn

Design of binderless grinding wheel with positive rake angle and fabrication used femtosecond laser ablation for grinding soft and brittle crystals

Abstract: Recent research has proved that precision grinding method can be used for machining the soft and brittle crystals, such as KDP, KTP, and LN et al, achieving much higher process efficiency than the single-point diamond cutting method. However, poor ground surface quality and impurity embedding are encountered when grinding these materials. In this paper, a binderless diamond grinding wheel with positive rake angle of cutting edges is innovatively designed and fabricated by femtosecond laser ablation on CVD diamond. To evaluate the effects of cutting edge rake angle on the grinding performance, two grinding wheels with 5º and 0º rake angles are fabricated. Grinding outputs of these two wheels, including ground surface roughness, surface microstructure and grinding forces for grinding KDP crystal are compared and analyzed. It is found that, positive rake angle effectively improved the ground surface quality, i.e. the ground surface roughness achieved using the wheel with 5º rake angle is about 1/10 of that obtained using the wheel with 0º rake angle. The positive rake angle wheel also effectively reduced the level of grinding forces and specific grinding energy. The grinding forces using the wheel with 5º rake angle are about 2/3 of that with 0º rake angle. It is also found that the wear depth of the binderless diamond grinding wheel with 5º rank angle is about 30 μm, with about 20 μm blade corner radius, and the wear depth of the wheel with 0º rank angle is about 20 μm, with about 10 μm blade corner radius, after removing 1000 mm^3 KDP material.

Keyword: positive rake angle; binderless grinding wheel; femtosecond laser ablation; CVD diamond; grinding performance; KDP crystal

1. Introduction

Optical crystal materials, such as KDP, KTP, and LN et al. are widely applied in semiconductor and laser industries [1-3]. In particular, KDP is an irreplaceable optical element in the Inertial Confinement Fusion (ICF) devices, due to its large diameter and excellent non-linear opto-electronic characteristics [1]. However, because of their softness, brittleness and sensitivity to thermal loads, these crystals are recognized as the most difficult-to-cut materials. According to previous studies, single point diamond turning (SPDT) is considered to be an ideal method for machining these materials [4-8]. Fuchs et al. produced finished KDP parts with no need for additional surface polishing, with surface roughness better than 8-Å RMS and 36-Å P-V [4]. Namba et al. use a single point diamond tool with rake angle of -25° achieved super smooth surface of RMS of 1.09 nm on a KDP test piece [5]. However, the machining efficiency of typical SPDT process is rather low, and often companied with severe wear issues of the diamond cutters. Recent research works have proved that grinding method is capable to achieve high process efficiency and low damage level for machining these crystal materials [9-11], whilst the performance of the grinding tool is crucial to ensure the success of soft crystal grinding. Qu et al. use a resin-bonded diamond grinding wheel to remove the surface material of KDP components with high efficiency for fixing the crystal axis [11]. However, impurity embeding and poor ground surface quality are encountered when using the traditional grinding wheels.

Development of novel binderless grinding wheel would provide an effective process tool to avoid grit and binder embeddings onto the crystal surface. Chemical vapor deposition (CVD) diamond is selected in this research as the abrasive layer for making the binderless grinding wheels, due to the availability of large size CVD diamonds and reasonable material strength and toughness [12-15]. To remove the unevenly distributed sharp grain protrusions on the original growth surface, CVD diamond needs to be polished and laser ablated to obtain the cutting edges with controllable and regular sizes. Butler-Smith had carried out a series of researches on laser ablation of CVD diamond cutting tools [16-19]. Butler-Smith fabricated triangular prism, pyramid and hexagonal prism micro-arrays with a size of 500 μm on the surface of CVD diamond by Nd: YAG Q-switched pulsed laser, and then designed and fabricated a micro-grinding tool, which has significantly excellent redress life for grinding Ti-6Al-4V. However, a graphite layer is produced on the surface of the micro-grinding tool due to laser thermal damage. The degree of graphitization of laser ablation become serious when increase the density and decrease the size of cutting. Femtosecond laser, which has extremely short pulse time and ultra-high peak power can used to avoid laser thermal damage and laser-ablate CVD diamond to obtain a binderless grinding wheel with dense and less than 100 μm cutting edges [20-23].

The cutting rake angles formed by the irregular shaped and orientated abrasive grits on traditional grinding wheels are typically in the range of -60°--70°. Machining with negative-rake tools would increase the magnitudes of cutting forces, the specific cutting energy and also the degree of surface and sub-surface material deformation, as shown in the study over a wide range of negative rake angle grinding wheels using molecular dynamics simulation [24]. It is found in a coupled thermomechanical dynamic analysis, that negative rake angle tends to cause thermal damage on the grinding wheel and workpiece [25]. Fu et al. (2016) found that a larger magnitude of negative rake angle can increase the maximum undeformed chip thickness of cutting edges and reduce ground surface quality when grinding Ti-6Al-4V by CBN grinding wheel [26].

In this study, a binderless diamond grinding wheel with positive rake angle cutting edges is designed and fabricated by femtosecond laser ablation on CVD diamond. To evaluate the effects of rake angle of cutting edge on the grinding performance, two grinding wheels with 5º and 0º rake angles are fabricated. Grinding outputs of these two wheels, including ground surface roughness, surface microstructure and grinding forces for grinding KDP crystal are compared and analyzed.

2. Design of binderless diamond grinding wheel

2.1 Grinding mechanism

The design of experiment is shown in Fig. 1a. The grinding wheel rotates around the spindle at high speed (grinding wheel speed v_s), the longitudinal feed (grinding depth a_p) is realized by changing axial spindle positions. Workpiece fixed on the worktable with a clamp and moves with the worktable (worktable speed v_w). In the grinding process, outer rings of abrasive layer contact with the workpiece to remove most materials at first, which plays a major cutting role. Other abrasive layer remove residual materials to improve surface quality to a certain level. The cutting edges are divided into n rings from outermost to innermost. Arranged the outermost ring as the first ring, and orderly count towards the innermost ring, *nth* ring. Set the center point of the grinding wheel as the origin of coordinates, and the worktable feed direction as the Y-axis to establish the rectangular moving coordinate system oxy. Number the point on the positive Y-axis as the first cutting edge, and count counterclockwise to the *mth* cutting edge. The cutting edge trajectories, which is on the *ith* ($1 \le i \le n$) ring and *jth* ($1 \le j \le m$) cutting edge can be calculated according to formulas (1-2):

$$x_{ij} = \left(r - (i-1) \cdot \Delta \mathrm{d}_i\right) \sin(\omega t - (j-1)\varphi) \quad (1)$$

$$y_{ij} = \left(r - (\mathrm{i}-1) \cdot \Delta \mathrm{d}_i\right) \cos(\omega t - (\mathrm{j}-1)\varphi) + v_w t \quad (2)$$

The feeding distance per revolution of one cutting edge is:

$$\Delta d_{si} = 2\pi r_i v_w / v_s \quad (3)$$

The track spacing of two circumferential cutting edges on the same ring:

$$\Delta d_{mi} = \varphi r_i \frac{v_w}{v_s} \quad (4)$$

The distance between the grain marks is:

$$\Delta d = \min\left\{\Delta d_{si}, \Delta d_{mi}, \Delta d_r\right\} \quad (5)$$

Where: r_i is the radius of *ith* ring ($r_n < r_i < r$); ω is angular velocity of a grinding wheel; Δd_r is the distance between adjacent rings; φ is the angle between adjacent cutting edges on the same ring.

According to formula 5, the distance between the grain marks Δd is determined by the machining parameters (v_w, v_s), φ and Δd_r. By analyzing Δd, the width of the main grinding zone in the abrasive layer can be determined, and the machining surface of this zone is in the side face of the workpiece (as shown in Fig. 1b). Maximun undeformed chip thickness of the main cutting edges can be calculated according to formula 6, where L ($L = \varphi r$) is the distance of cutting edges (as shown in Fig. 1c).

$$h_m = \frac{v_w}{v_s} L = \Delta d_m \quad (6)$$

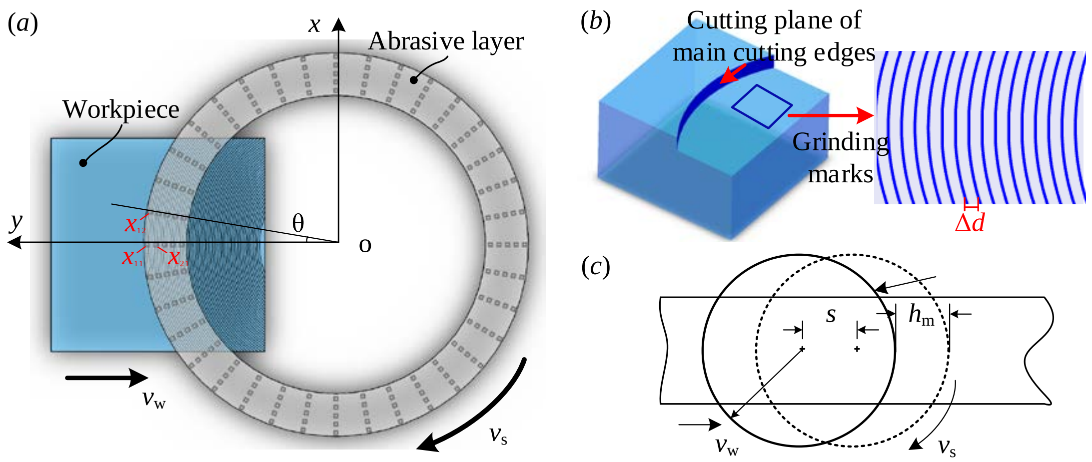

Fig. 1 Vertical surface grinding (*a*) the distribution model of grits, (*b*) surface of the main grinding zone and the grain marks, and (*c*) maximum undeformed chip thickness of the main cutting edges

Fig. 2 shows the marking angles of the main cutting edges with different shapes in the orthogonal plane reference frame. The orthogonal plane reference system is composed of a cutting plane (P_s), base plane (P_r) and principal section (P_o). The rake angle r_o is in the principal section. As shown in Fig. 2a, the cutting edges in the outermost ring is a triangular prism, and $r_o > 0°$. As shown in Fig. 2b, the cutting edges in the outermost ring is a quadrangular prism, and $r_o \leq 0°$.

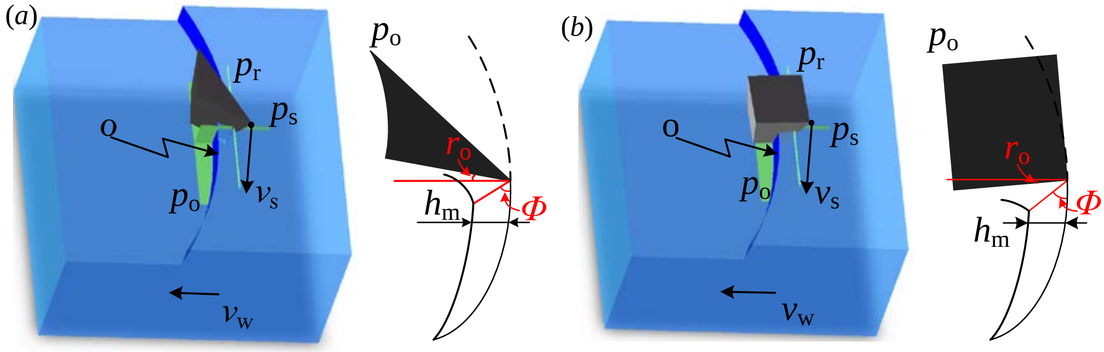

Fig. 2 Marking angles of the main cutting edges with different shapes in the orthogonal plane reference frame (*a*) triangular prism and (*b*) quadrangular prism

2.2 Binderless diamond grinding wheel

The designed cutting edges of grinding wheel I is shown in Fig. 3a. Outermost cutting edges are isosceles triangular prism whose waist length is 300 μm and apex angle is 100°. After comprehensively considering the cutting performance and tool wear, the γ_o is designed to 5°. Other cutting edges are quadrangular prism with a side length about 35 μm, cutting edges density $C_{G,A}$ about 14 mm^{-2}. The designed cutting edges of the grinding wheel II is shown in Fig. 3b. The outermost cutting edges are quadrangular prism with a side length about 300 μm, and the γ_o as 0°. The other cutting edges are the same as on grinding wheel I.

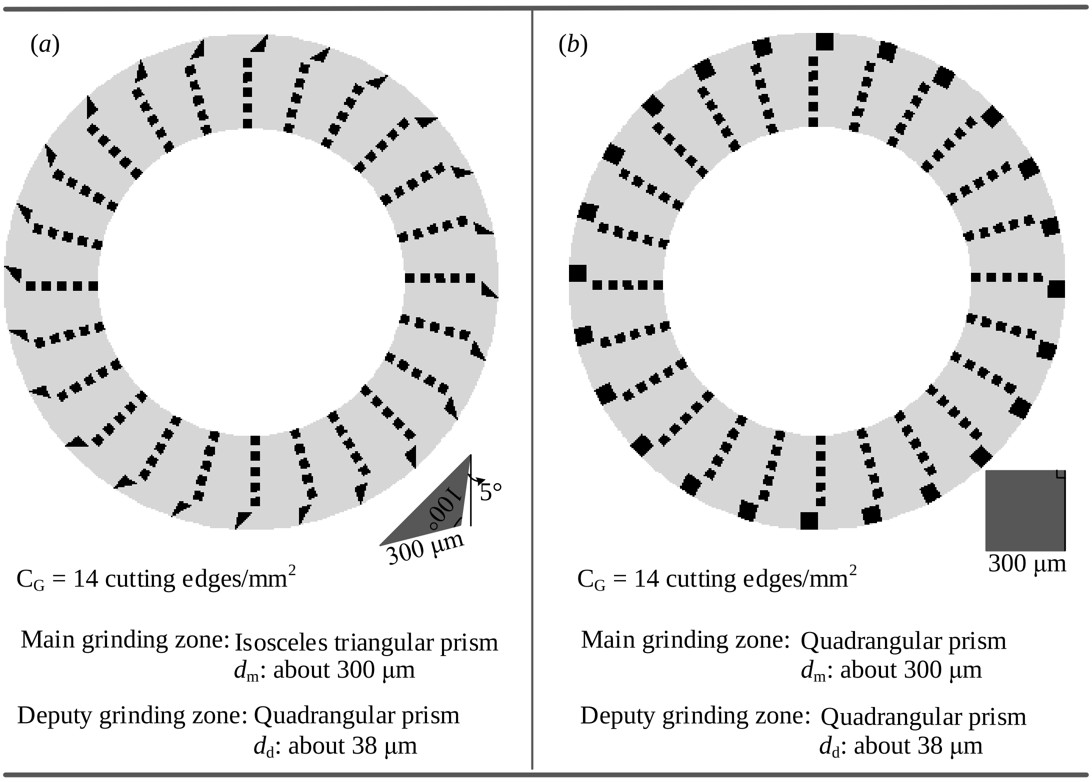

Fig. 3 Design of binderless diamond gringing wheels (*a*) I and (*b*) II

3. Fabrication of binderless diamond grinding wheel

3.1 Manufacturing processes

To manufacture the binderless diamond grinding wheel, firstly, CVD diamond with good thermal and mechanical properties comparable to natural diamond is selected as the material for abrasive layer. The diameter of CVD diamond can achieve 200 mm diameter and 3 mm thickness, which not only meets the requirements of the abrasive layer, but also the strength, toughness and wear resistance of the cutting edges. Then, polish the CVD diamond to meet the requirements of surface precision, and cut into a ring. The roughness Ra is from before polishing 6.0 μm to 80 nm after polishing. After that, a large number of cutting edges with certain arrangement, shape and size are constructed on the abrasive layer by femtosecond laser ablation. Finally, the CVD diamond abrasive layer is attached with the tool holder by adhesive bonding or welding. Before grinding, measuring the round runout of the binderless grinding wheel and controlled it within 10 μm. The specific manufacturing process is shown in

Fig. 4.

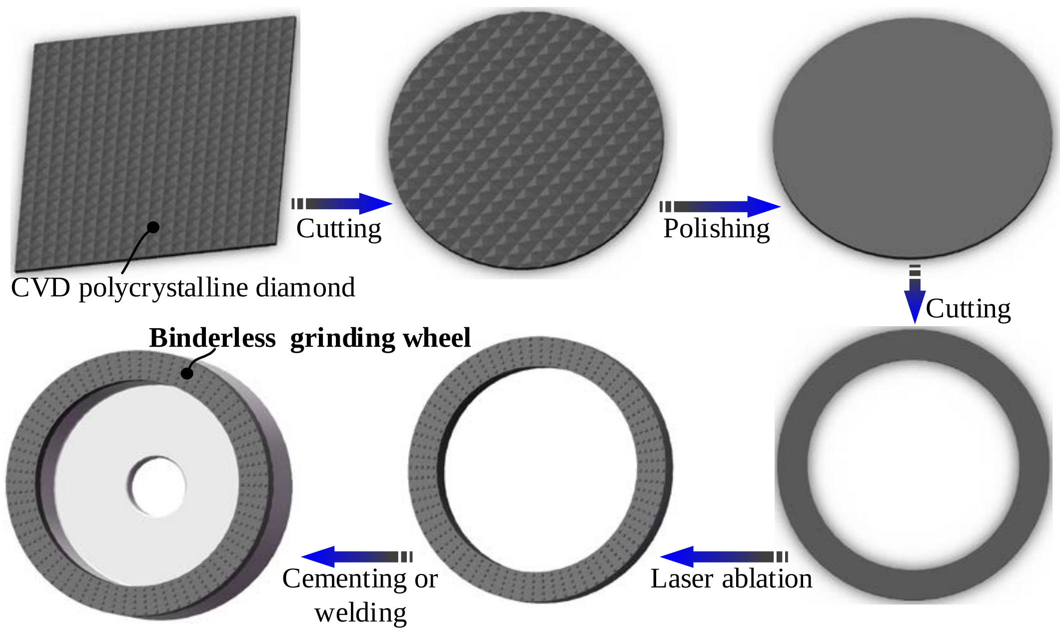

Fig. 4 Manufacturing processes of binderless diamond grinding wheel

3.2 Femtosecond laser ablation platform

Fig. 5 is the platform of femtosecond laser ablation, which is mainly composed of femtosecond laser, 2D scanning galvanometer and a mobile platform. The focal length of the 2D scanning galvanometer is 174 mm and 100×100 mm scanning scope. Pulsed femtosecond laser can output laser wavelength of 343 nm, 515 nm and 1030 nm through frequency multiplier, with average power of 35 W and maximum energy of single pulse ≥200 uJ. The specific performance parameters are shown in table 1.

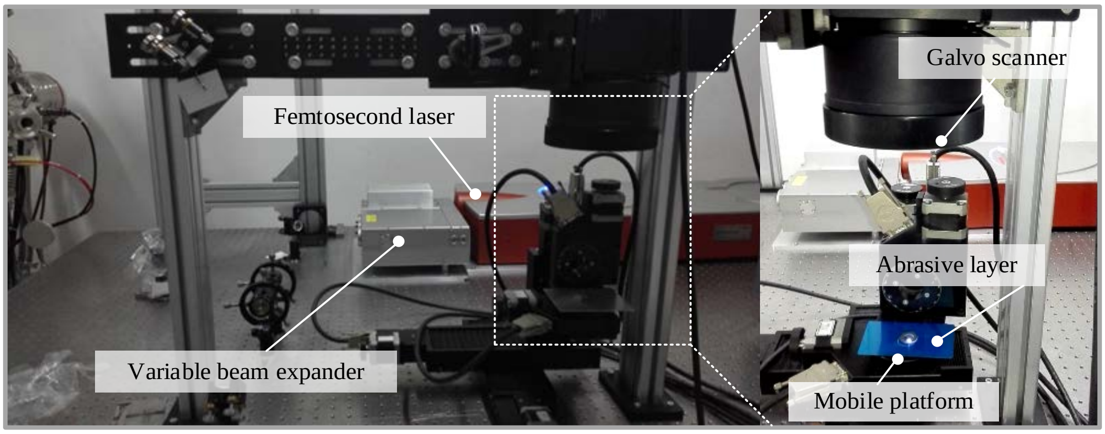

Fig. 5 The platform of femtosecond laser ablation

Table 1 Performance parameters of femtosecond laser

Average power	0-35 W
Repetition frequency	175 kHz
Pulse width	≥250 fs
Diameter of laser spot	30 μm
trigger mode	Pulsed
Wavelength	343 nm, 515 nm, 1030 nm

3.3 Laser ablation path

Different from milling tools, binderless diamond grinding wheels surface have a large number of cutting edges with micro-size, dividing CVD diamond ring into several ablation unit to avoid response delay of laser beam in processing. After scanning a unit, the laser beam successively scans the next unit along the circle, until the entire ring is scanned and an ablation cycle is completed. Femtosecond laser pulse width of 250 fs, average power of 11.1 W, scanning speed of 2 m/s, repetition frequency of 175 kHz, and 12 μm adjacent laser ablation track spacing are selected as the technological parameter combination to meet the design parameters.

Fig. 6 shows the laser ablation path of grinding wheels I and II include six repeating units. Considering the effect of diameter of laser spot (about 30 μm), the size of cutting edges in the laser ablation path is larger than that of the designed cutting edges (about twice size of the diameter of laser spot). As shown in Fig. 6a, the outermost cutting edges are isosceles triangular prism with waist length of 360 μm, apex angle of 100º and rake angle γ_o of 5º. Other cutting edges are quadrangular prism with a side length of 100 μm. As shown in Fig. 6b, the outermost cutting edges are quadrangular prism with a side length of about 360 μm and rake angle of 0º. Other cutting edges are as same as the grinding wheel I. Because of the difference in shape and size of the cutting edges between the outermost and the inner zone, separate zones to complete laser ablation. The ablation cycle is performed 100 times for the outermost zone and 50 times for the inner zone.

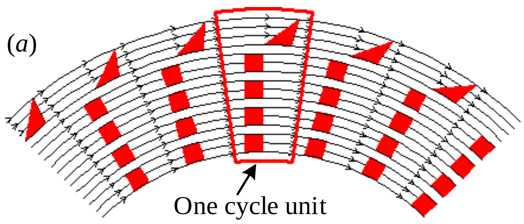

Fig. 6 Laser ablation of grind wheel (*a*) I and (*b*) II

3.4 Topography of binderless diamond grinding wheel

Fig. 7 shows the topography of the binderless diamond grinding wheels with an outer diameter of 16 mm and an inner diameter of 10 mm after laser abrasion. As shown in Fig. 7a, the outermost cutting edges are isosceles triangular prism with waist length of 300 μm, apex angle of 100º, protruding height of 100 μm and rake angle γ_o of 5º. Other cutting edges is quadrangular prism with a side length of 38 μm, protruding height of 20 μm and the cutting edges density $C_{G,A}$ about 14 mm^{-2} . As shown in Fig. 7b, the outermost cutting edges are quadrangular prism with side length of about 400×300 μm and rake angle of 0º. Other cutting edges are same as grinding wheel I.

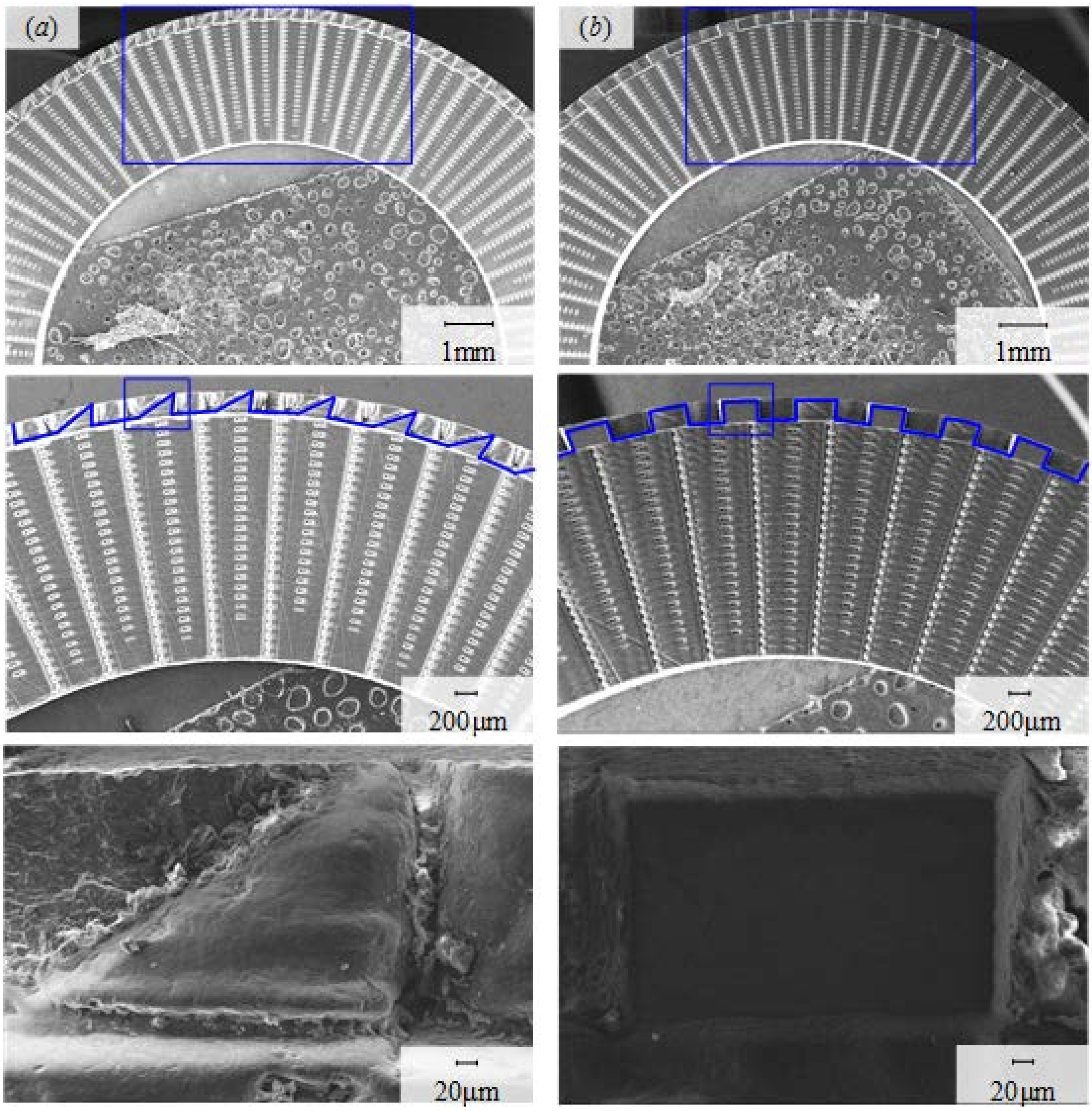

Fig. 7 Topography of grinding wheel (*a*) I , and (*b*) II

4. Grinding performance experiment

4.1 Work-piece

To evaluate the influence of rake angle on grinding performance, KDP crystal with size of 20×20×10 mm^3 is selected as a work-piece, which is a typical soft and brittle crystal.

4.2 Grinding platform

As shown in Fig. 8, a precision CNC grinding machine is used as the grinding platform, which has six CNC axes (X, Y, Z, U, A, and C). The movement control resolution of X and Y axes are 0.1 mm, and the positioning accuracy of the Z–axis is within 0.05 mm.

Fig. 8 Grinding platform

4.3 Measurements

Kistler9257B dynamometer with PCI6115 acquisition card is applied to retrieve grinding normal and tangential grinding forces (F_n, F_t). The sampling frequency is 5000 Hz. VHX-1000, KEYENCE is used to observe the ground surface morphology at the work-piece center at 500 times magnification. Talysurf PGI 1240, Taylor-Hobson is used to measure the surface roughness along the direction perpendicular to the grain marks. The sample length is 0.8 mm and the evaluation length is 4 mm.

4.4 Grinding parameters

To comprehensively evaluate the grinding performance of the grinding wheel I and II, the grinding results under different grinding speed v_s and worktable speed v_w were investigated. Grinding parameters are shown in table 2.

Table 2 Grinding parameters

Grinding speed	Worktable speed	Grinding depth	Maximum undeform chip thickness

	v_s (m/s)	v_w (mm/s)	a_p (μm)	h_m (μm)
1	3	2	10	0.4
2	6	2	10	0.2
3	6	4	10	0.4
4	6	6	10	0.6
5	6	8	10	0.8
6	6	10	10	1

5. Experimental results

5.1 Surface roughness R_a

Fig. 9 shows the surface roughness R_a of two grinding wheels under different grinding parameters, including v_w=2 mm/s, a_p=10 μm, in Fig. 9a v_s=3 m/s, 9b v_s=6 m/s. As shown in Fig. 9a, the R_a of the grinding wheel I is about 0.2 μm, and the R_a of grinding wheel II is about 2 μm. As shown in Fig. 9b, the R_a of the grinding wheel I is about 0.17 μm, and the R_a of grinding wheel II is about 1.4 μm. The results show that the R_a of the surface ground by the grinding wheel I is better than that of grinding wheel II under the same grinding parameters. As the grinding speed increases, the maximum undeform chip thickness decreases accordingly. Therefore, increasing the grinding speed can further improve the surface roughness R_a.

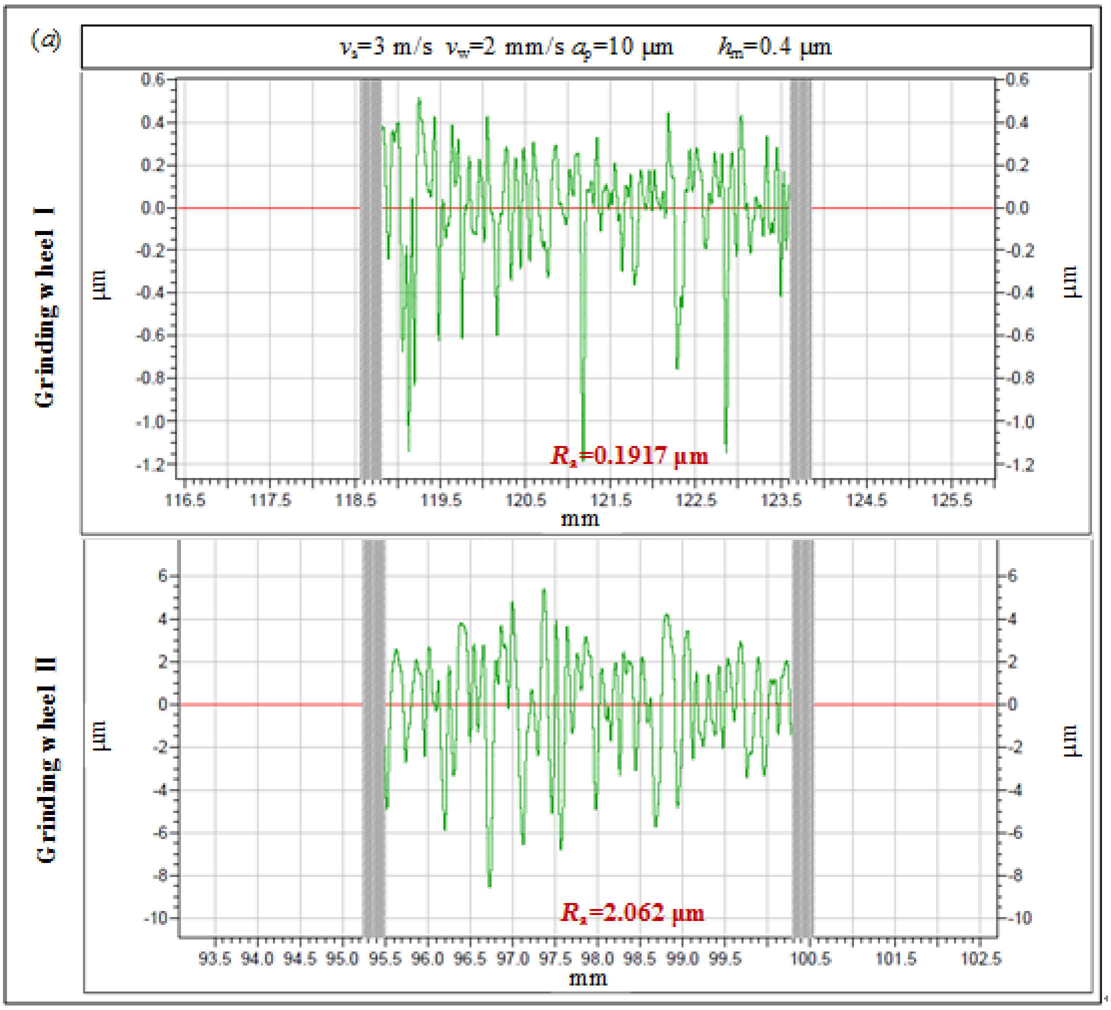
(a)
v_s=3 m/s v_w=2 mm/s a_p=10 μm h_m=0.4 μm
Grinding wheel I
μm
R_a=0.1917 μm
mm
Grinding wheel II
R_a=2.062 μm

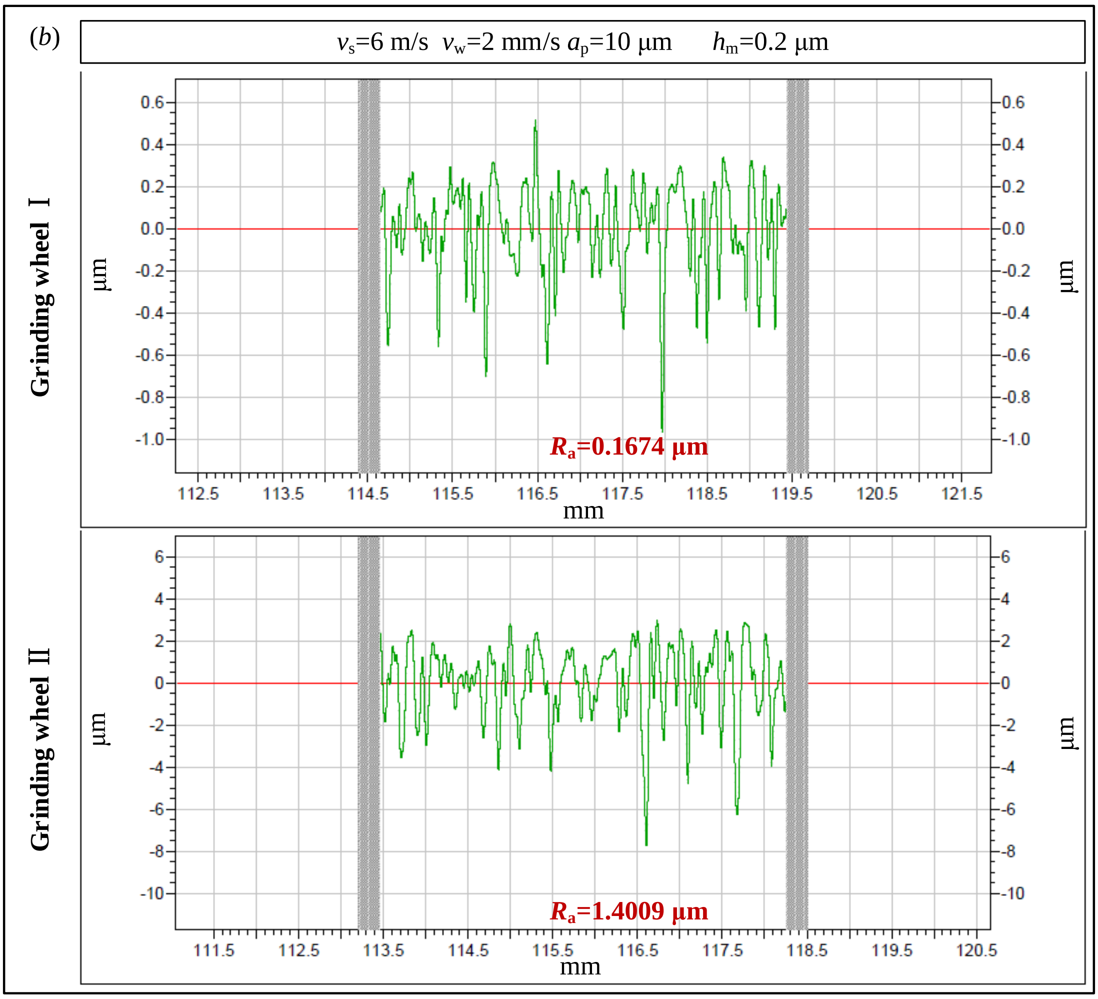

Fig. 9 Surface roughness under v_w=2 mm/s, a_p=10 μm, (a) v_s =3 m/s and (b) v_s=6 m/s

5.2 Surface microstructure

Fig. 10 shows the surface microstructure of the grinding wheels I and II under different grinding parameters, including v_w=2 mm/s, a_p = 10 μm, 10(a) v_s=3 m/s, Fig. 10(b) v_s=6 m/s. As shown in Fig. 10, the surface of the grinding wheel I is composed of fine plastic grooves and fine brittle spalling pits along the grooves. The surface of the grinding wheel II consists of a large of brittle spalling pits. The results show that the surface microstructure ground by the grinding wheel I is better than that of the grinding wheel II under the same grinding parameters. As the increase of the grinding wheel speed, the maximum undeform chip thickness decreases accordingly, the plastic marks on the grinding surface increase and the brittle spalling pits decrease. Therefore, improving the grinding speed v_s can further improve the surface processing quality.

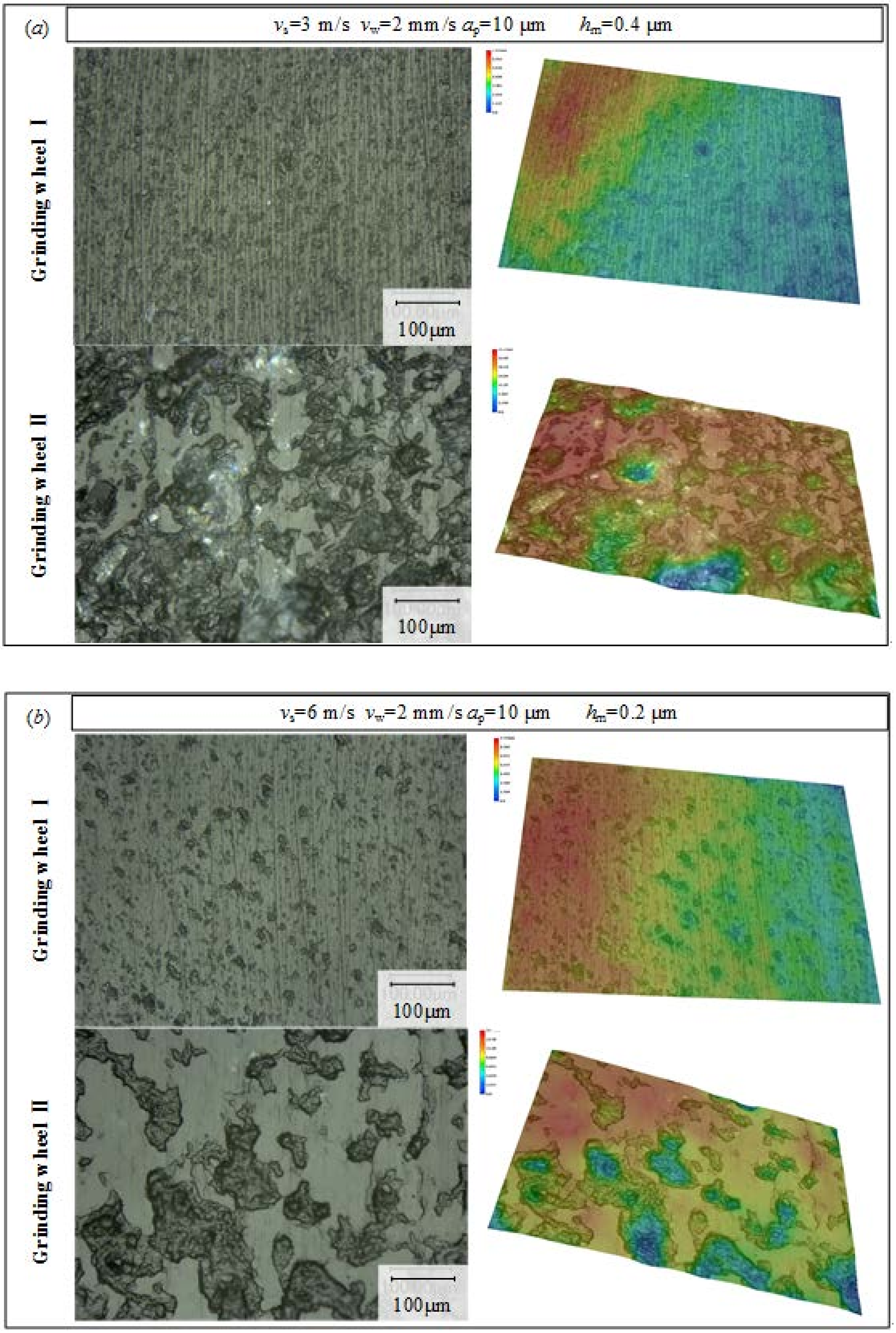

Fig. 10 Surface microstructure of work-piece under v_w=2 mm/s a_p=10 μm (*a*)

v_s=3 m/s, (*b*) v_s=6 m/s

5.3 Grinding forces

Fig. 11 shows the normal grinding force F_n, tangential grinding force F_t and the ratio of F_n to F_t of the grinding wheels I and II under different grinding parameters, including v_s=6 m/s, a_p=10 μm, v_w=2~10 mm/s. As shown in Fig. 11 a and b, the grinding forces of the grinding wheels I and II increase with the increasing worktable speed. The grinding forces of grinding wheel I are less than grinding wheel II, and the growth rate of grinding wheel I is greater than the II. As shown in Fig. 11c, with the increase of worktable speed, the grinding force ratio of grinding wheel I and II decreases, but the reduction range is less 1. The grinding force ratio of grinding wheel II is about 5.5, a slightly higher than grinding wheel I (4.5). As the worktable speed increases, the maximum undeformed chip thickness and the grinding forces increase. Therefore, reducing the worktable speed effectively reduces the grinding forces.

(*a*)

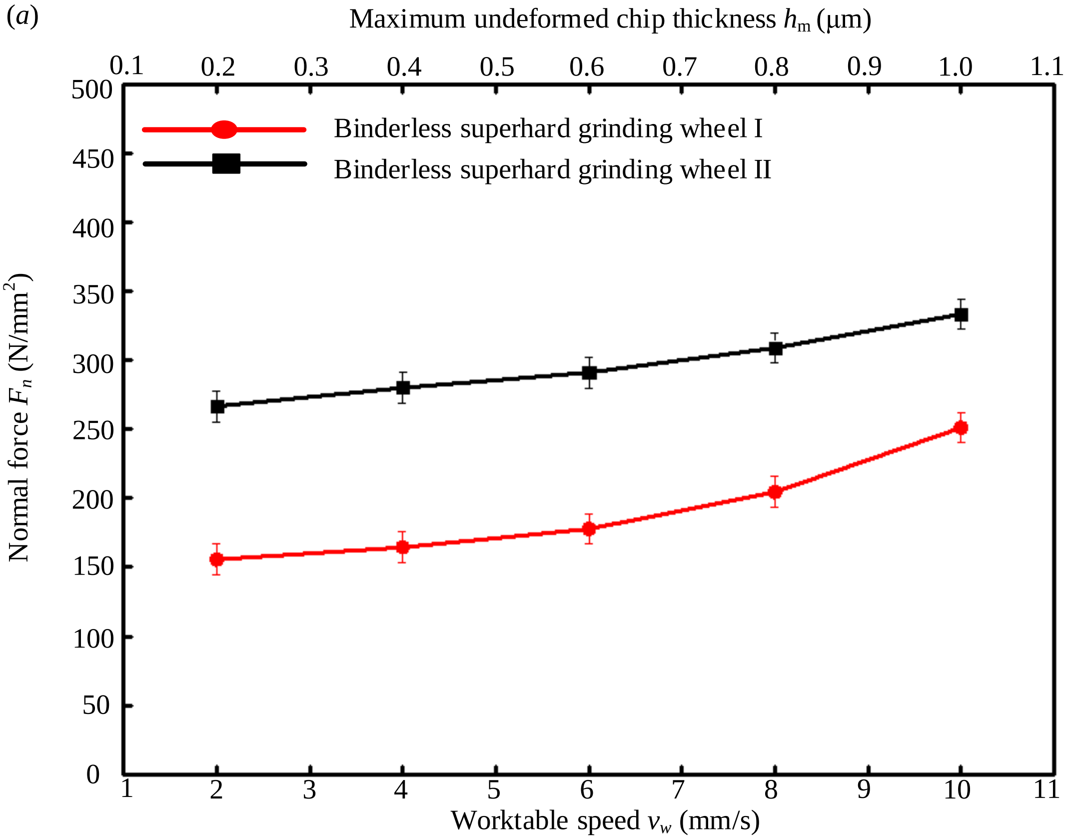

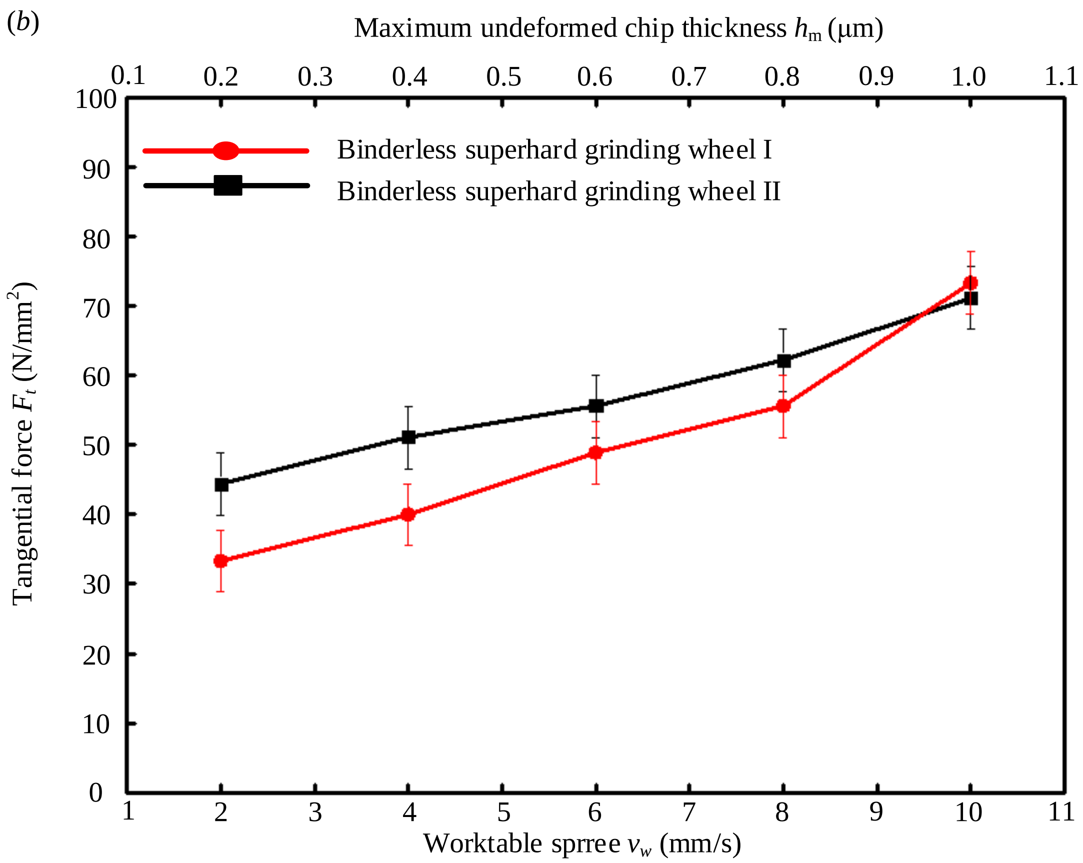
(b)
Maximum undeformed chip thickness hm (μm)
0.1
0.2
0.3
0.4
0.5
0.6
0.7
0.8
0.9
1.0
1.1
100
90
80
70
60
50
40
30
20
10
0
Binderless superhard grinding wheel I
Binderless superhard grinding wheel II
Tangential force Ft (N/mm2)
1
2
3
4
5
6
7
8
9
10
11
Worktable sprree vw (mm/s)

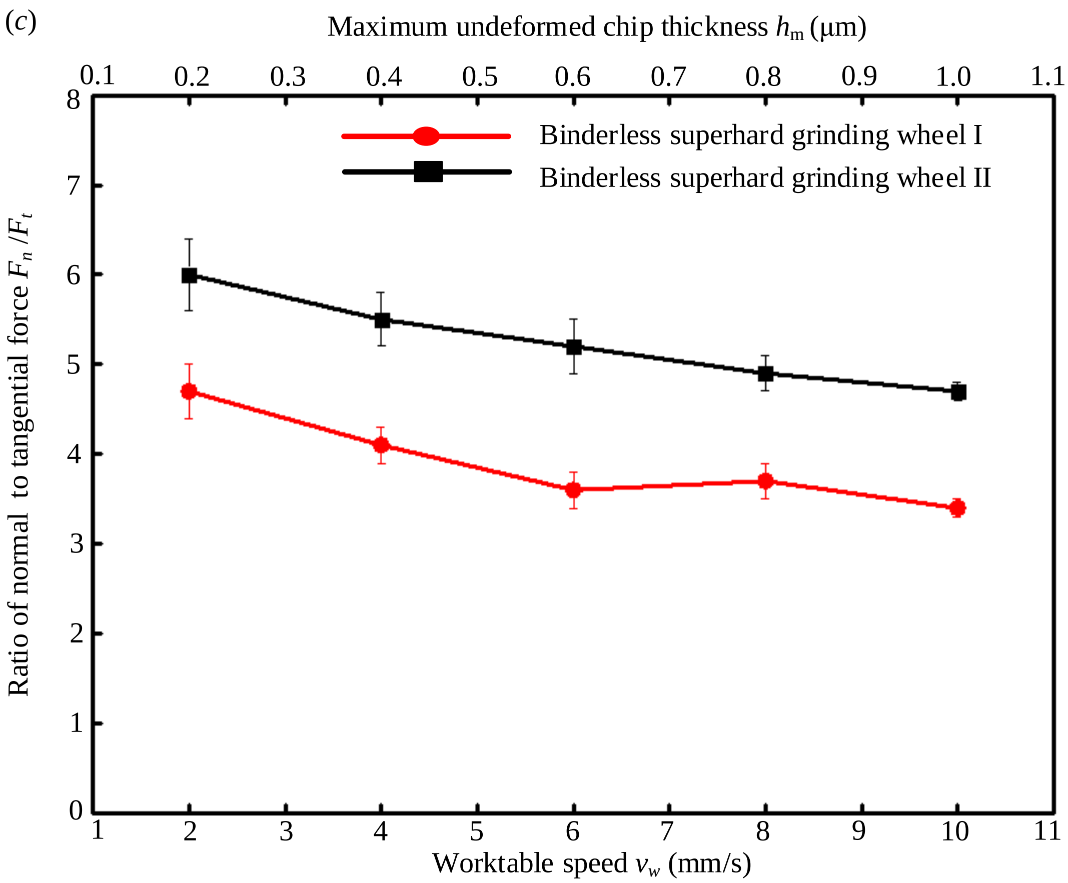

Fig. 11 Grinding forces (*a*) normal force, (*b*) tangential force and (*c*) ratio of normal to tangential force

5.4 Specific grinding energy

Specific grinding energy (e_s) is an important index to evaluate grinding performance of a grinding wheel. Reducing the e_s reduces the heat flux. The e_s can be calculated using tangential force (formula 7) [27]. As shown in Fig. 12, the specific grinding energy, e_s, for both wheel I and II, reduced exponentially when increasing the worktable speed. The e_s of grinding wheel I is less than that of the grinding wheel II under the same grinding parameters. Therefore, the heat flux of grinding wheel I is less than grinding wheel II under the same grinding parameters. Increasing worktable speed further reduces the specific grinding energy.

$$e_s = \frac{F_t v_s}{v_w a_p b} \quad (7)$$

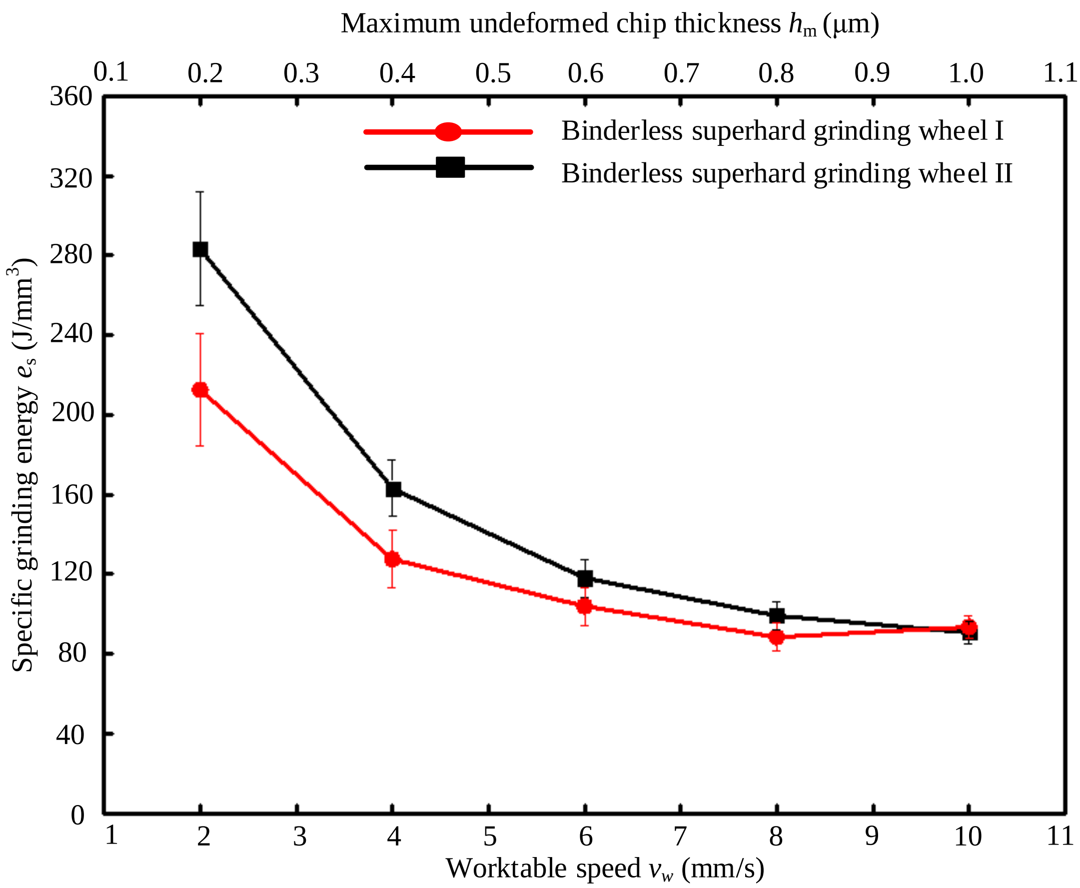

Fig. 12 Specific grinding energy

6. Discussion

The angle between two adjacent cutting edges φ is about 5 ° and the radial distance between two adjacent rings Δd_r is about 500 μm, which cutting edges located at the outermost rings of grinding wheels I and II. Take 6 groups of grinding parameters (a_p=10 μm, v_w=2 mm/s, v_s =3 m/s) for example, the per revolution feeding distance of one cutting edge Δd_{s1} is about 72 μm and the track spacing between two circumferential cutting edges Δd_{m1} is about 1 μm, which cutting edges located on the outermost according to formula 1 to 5. Thus, it can be seen that the space between two adjacent cutting edges Δd_m is far less than the feed distance Δd_s and the radial spacing between two adjacent rings Δd_r. Therefore, it can be determined that the main grinding area is the outermost ring. The rake angle located on the outermost of grinding wheel I has positive rake angle (5º), which is sharper than grinding wheel II (0º). Therefore, grinding wheel I can obtain better surface roughness R_a (as shown in Fig. 9) and surface microstructure and quality (as shown in Fig. 10) with low grinding forces (as shown in Fig. 11).

Although the larger positive rake angle can effectively improve the grinding performance, the edge strength is relatively poor. Fig. 13 shows the wear of grinding wheel I and II after removing of 1000 mm^3 KDP crystal. The wear depth of grinding wheel I is about 30 μm, blade radius r is about 20 μm. The wear depth of grinding wheel II is about 20 μm, blade radius r is about 10 μm. Although the cutting edges located on the outermost ring of grinding wheels I and II both have wear, but the wear of grinding wheel I is more apparent.

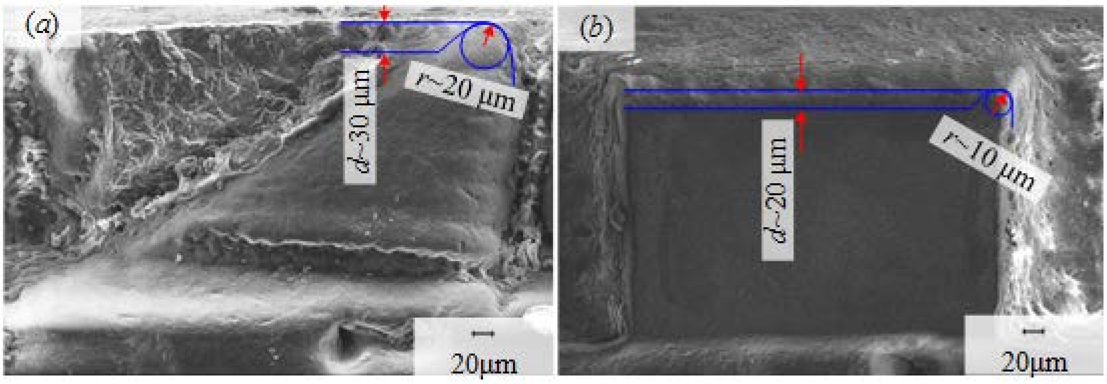

Fig. 13 Cutting edge wear of grinding wheel (*a*) I, and (*b*) II

7. Conclusion

In this study, binderless diamond grinding wheels with zero and positive rake angle cutting edges are innovatively designed and fabricated by femtosecond laser ablation on CVD diamonds. The grinding performance of these two wheels for grinding the KDP crystal, including ground surface roughness, surface microstructure, grinding forces, and the types of grinding wheel wear are investigated. The main research conclusions are as follows:

1. For vertical surface grinding, abrasive layer can be divided into two zones, in which the cutting edges located on the outer rings remove most of the workpiece material and play a main cutting role. The rake angle can be designed based on analyzing the abrasive trajectories of cutting edges and cutting angles.

2. Cutting edges with high density and micronsize can be constructed, by properly planning laser ablation path and selecting machining parameters.

3. Larger positive rake angle of cutting edges located on the outermost ring can effectively reduce the surface roughness R_a, improve the surface microstructure and surface quality, and reduce the grinding forces and grinding energy.

4. Two binderless diamond grinding wheels both have abrasion wear, larger positive rake angle weakens the cutting edge slightly. The wear depth of the binderless diamond grinding wheel with 5 º rank angle is about 30 μm, blade radius is about 20 μm, and the wear depth of binderless diamond grinding wheel with 0 º rank angle is about 20 μm, blade radius is about 10 μm after removal 1000 mm^3 KDP crystal.

Acknowledgements

This work was supported by the National Science and Technology Major Project of China [No. 2014ZX04001191].

References

[1] Bespalov VL, Bredikhin VI, Ershov VP, Zilberberg VV. Perspectives for creation of highly effective technology for fabricating KDP and KD*P crystals for ICF. Proceedings of SPIE 1997; 3047: 899-902.

[2] Kustarci A, Arslan D, Kaya B. Effects of three different irrigating solutions and KTP laser irradiation on apical leakage: an electrochemical study. Acta Odontologica Scandinavica 2012; 70:377–383.

[3] Randles AB, Kuypers JH, Esashi M, Tanaka S. Application of Lithium Niobate Etch Stop Technology to SAW Pressure Sensors. IEEE Ultrasonics Symposium 2008; 1124-1127.

[4] Fuchs BA, Hed PP, Baker PC. Fine Diamond Turning of KDP Crystals. Applied Optical 1986; 25: 1733-1736.

[5] Namba Y, Katagiri M, Nakatsuka M. Single point diamond turning of KDP inorganic nonlinear crystal for laser fusion. The Japan Society for Precision Engineer 1998; 64: 1487-1491.

[6] Wang SF, An CH, Zhang FH, Wang J, Lei XY, Zhang JF. An experimental and theoretical investigation on the brittle ductile transition and cutting force anisotropy in cutting KDP crystal. International Journal of Machine Tools & Manufacture 2016; 106; 98–108

[7] Tie GP, Dai YF, Guan CL, Zhu DC, Song B. Research on full-aperture ductile cutting of KDP crystals using spiral turning technique. Journal of Materials Processing Technology 2013; 213; 2137–2144

[8] Tie GP, Dai YF, et al. Research on subsurface defects of potassium dihydrogen phosphate crystals fabricated by single point diamond turning technique. Optical Engineering 2013; 52; 254-260

[9] Namba Y. Ultra-precision Grinding of Optical Materials for High Power Lasers, J. Proceedings of SPIE 1998; 3244; 320-330

[10] Chen DS, Chen JH, Wang BR. A hybrid method for crack-less and high-efficiency ultra-precision chamfering of KDP crystal. The International Journal of Advanced Manufacturing Technology 2016; 87; 293-302

[11] Qu MN, Xie GZ, Jin T, Cai R, Lu AG. Realization of high efficiency and low damage machining of anisotropic KDP crystal by grinding. Precision Engineering 2019; 55: 464-473.

[12] Laikhtman A, Avigal Y, Kalish R, Breskin A, Chechik R, Shefer E, Lifshitz Y, Hoffman A. Surface quality and composition dependence of absolute quantum photoyield of CVD diamond films. Diamond and Related Materials 1999; 8: 725–731.

[13] Brinksmeier E, Mutlugünes Y, Antsupov G, Rickens K. New Tool Concepts for Ultra-Precision Grinding. Key Engineering Materials 2012; 516: 287-292.

[14] Harniman RL, Fox OL, Janssen W, Drijkoningen S, Haenen K, Paul WM. Direct observation of electron emission from grain boundaries in CVD diamond by PeakForce-controlled tunnelling atomic force microscopy. Carbon 2015; 94: 386-395.

[15] Malshe AP, Park BS, Brown WD, Naseem HA. A review of techniques for polishing and planarizing chemically vapor-deposited (CVD) diamond films and substrates. Diamond and Related Materials 1999; 8: 1198–1213.

[16] Butler-Smith PW, Axinte DA, Daine M. Preferentially oriented diamond micro-arrays: A laser patterning technique and preliminary evaluation of their cutting forces and wear characteristics. International Journal of Machine Tools & Manufacture 2009; 49: 1175–1184.

[17] Butler-Smith PW, Axinte DA, Daine M. Ordered diamond micro-arrays for ultra-precision grinding—An evaluation in Ti–6Al–4V. International Journal of Machine Tools & Manufacture 2011; 51: 54–66.

[18] Butler-Smith PW, Axinte DA, Daine M. Solid diamond micro-grinding tools: From innovative design and fabrication to preliminary performance evaluation in Ti–6Al–4V. International Journal of Machine Tools & Manufacture 2012; 59: 55–64.

[19] Butler-Smith PW, Axinte DA, Pacella. M, Fay MW. Micro/nanometric investigations of the effects of laser ablation in the generation of micro-tools from solid CVD diamond structures. Journal of Materials Processing Technology 2013; 213: 194-200.

[20] Chang G, Tu YL. The threshold intensity measurement in the femtosecond laser ablation by defocusing. Optics and Lasers in Engineering 2012;50:767–71 .

[21] Desautels L, Brewer C, Powers P, et al. Femtosecond index change mechanisms and morphology of crystalline materials. Phys Lett A 2009; 5: 583-91.

[22] Chen JX, Zhou XL, Lin SW, Tu YL. A prediction-correction scheme for microchannel milling using femtosecond laser. Optics and Lasers in Engineering 2017; 91: 115-23.

[23] Zhang P, Chen L, Chen JX, Tu YL. Material removal effect of microchannel processing by femtosecond laser. Optics and Lasers in Engineering 2017; 98: 69–75.

[24] Komanduri R, Chandrasekaran N, Raff LM. Some aspects of machining with negative-rake tools simulating grinding: a molecular dynamics simulation approach. Philosophical Magazine Part B 1999; 79(7): 955-968.

[25] Akbari M, Buhl S, Leinenbach C, Wegener, K. A new value for Johnson Cook damage limit criterion in machining with large negative rake angle as basis for understanding of grinding. Journal of Materials Processing Technology 2016; 234: 58-71.

[26] Fu D, Ding W, Yang S, Miao Q, Fu Y. Formation mechanism and geometry characteristics of exit-direction burrs generated in surface grinding of ti-6al-4v titanium alloy. The International Journal of Advanced Manufacturing Technology 2016; 89: 2299-2313.

[27] Malkin S. Grinding Technology: Theory and Application of Machining with Abrasives. New York. 1989